Marthe G. Guren[1,*], Henrik A. Sveinsson[1], Anders Malthe-Sørenssen[1] and François Renard[1,2]

[1]The Njord Centre, Departments of Geosciences and Physics, University of Oslo, Norway

[2]ISTerre, Univ. Grenoble Alpes, Grenbole INP, Univ. Savoie Mont Blanc, CNRS, IRD, Univ. Gustave Eiffel, 38000 Grenoble, France

*Corresponding author: Marthe Guren (m.g.guren@geo.uio.no)

Key Points:

- Dynamic tensile rupture propagation simulated in alpha-quartz using molecular dynamics simulations
- A path instability occurs when the rupture speed is greater than 15 % of the Rayleigh wave speed
- Microbranching may lead to a production of fragments with sizes below the grinding limit

Abstract

The creation of new fractures controls fault slip, produces rock damage, and contributes to the dissipation of energy during earthquakes. Pulverized rocks around faults contain grains with a wide range of sizes, but the mechanisms that produces nanoscale grains remain elusive. Using molecular dynamics simulations, we model tensile rupture propagation in alpha-quartz under conditions of stress that occur during earthquake propagation. Our results show that for rupture speeds below 15 % of the Rayleigh wave speed, the fracture propagates straight. At higher speeds, fracture propagation undergoes path instabilities with crack oscillations and microbranching. We show that microbranching can lead to nanoscale fragments. Energy dissipation occurs by the creation of fracture surfaces and material damage; the dissipated energy increases with rupture speed. This nanoscale mechanism of irreversible deformation during earthquake propagation conditions contributes to the energy budget of earthquakes, and damage production in fault zones.

Plain Language Summary

During the propagation of earthquakes, the creation of new fractures produces damage in the surrounding rock at all scales. However, the mechanism of nanoscale damage production remain enigmatic. For brittle materials, crack propagation may evolve from straight to a pattern that includes oscillations above a threshold rupture speed. Using -quartz as a representative material for crystalline rocks, we show that above 15 % of the Rayleigh wave speed, crack propagation involves oscillations and microbranching events during which two cracks propagate simultaneously until one branch dominates. The aborted branch and the propagating branch produce rock fragments with nanoscale dimensions.

1 Introduction

The propagation of dynamic fractures during earthquakes produces damage along faults and in the surrounding rock that may lead to rock pulverization under high strain rates (e.g., Dor et al., 2006; Doan et al., 2009). Pulverized rocks are characterized by multi-scale fractures (Rempe et al., 2013) and rock fragments with sizes ranging from sub-micrometers to centimeters, often having power-law size distributions (Sammis et al., 1987; Keulen et al., 2007; Muto et al., 2015). The observation of asymmetric damage zones in crustal faults may occur due to the propagation of ruptures along a bi-material interface, producing high tensile stresses on one side of the fault (e.g., Andrews, 2005; Ben-Zion and Shi, 2005; Reches and Dewers, 2005; Di Toro and Pennacchioni, 2005; Petley-Ragan et al., 2019). During dynamic rupture, the rock splits into fragments with a wide range of sizes. Previous work has suggested that some materials have a minimum fragment size achieved through grinding, i.e., the grinding limit (Kendall, 1978). For quartz, the grinding limit is 0.9 µm (Prasher, 1987); however, quartz grains with radius of 15 nm have been observed in experiments and naturally produced gouges (Keulen et al., 2007). The observation of rock fragments with dimensions below the grinding limit prompts a reexamination of the mechanical origin of these fragments. Here, we use molecular dynamics simulations to identify a mechanism that produces nanoscale damage caused by dynamic rupture and due to out-of-plane unstable crack propagation under tensile loading conditions.

A dynamic fracture may develop as a straight crack that propagates in a stable manner along a single fracture plane (e.g., Bouchbinder et al., 2014), or it may become unstable when the crack tip oscillates in the z-direction, which may lead to microbranching (e.g., Bleyer and Molinari, 2017). The type of propagation varies with rupture speed. At low speeds, fracture surface roughness may develop with three morphologies: mirror, mist, or hackle (Fineberg et al., 1991; Buehler, 2008). For mirrors, the crack propagates at low speeds creating a perfect cleavage, and as the speed increases, the crack surface changes from slightly rough (mist) to significantly rough (hackle). The mirror-mist-hackle regimes have been observed in experiments (e.g., Fineberg et al., 1991), as well as in models containing a perfect atomic lattice (e.g., Abraham et al., 1997; Buehler and Gao, 2006). Dynamic instabilities at the crack tip result in rupture propagation speeds below the Rayleigh wave speed, C_{R}, the rupture speed predicted for dynamic straight cracks by linear elastic fracture mechanics (Fineberg et al., 1991). The transition between the stable and unstable propagation regimes occurs when the crack tip speed exceeds a critical value that has been measured experimentally in several materials: $0.44C_{\mathrm{R}}$ for silica glass (Sharon and Fineberg, 1998), $0.44C_{\mathrm{R}}$ for polymethyl methacrylate (Fineberg et al., 1991; Sharon and Fineberg, 1996), and $0.34C_{\mathrm{R}}$ for neo-Hookean brittle gels (Livne et al., 2005). Above these critical rupture speeds, the crack deviates from a linear propagation and oscillate or branch into two or more cracks.

At the nanoscale, dynamic fractures nucleate when the breaking of an inter-

atomic bond starts an avalanche of subsequent bond breakage, resulting in the propagation of a crack across length scales. Crack instabilities have been observed all the way down to the nanoscale (e.g., Zhou et al., 1996). Molecular dynamics simulations of a two-dimensional homogenous brittle solid with linear elastic properties have shown that crack branching occurs when the rupture speed exceeds a critical value, similar to experimental observations. The first such study reported a critical rupture speed of $0.35\,C_{\mathrm{R}}$ (Zhou et al., 1996), and a later study indicated a value of $0.73\,C_{\mathrm{R}}$ (Buehler and Gao, 2006). The difference between these critical speeds can be attributed to the shape of the interatomic potential used in the simulations. Zhou et al. (1996) used a Morse pair potential while Buehler and Gao (2006) used a smoothed biharmonic potential, which allows a hyperelastic zone size and the cohesive force between interacting atoms to be tuned. Bueher and Gao (2006) found that hyperelasticity and the ratio between the distance of maximum interatomic attraction and the equilibrium interatomic distance controls the critical rupture speed.

Here, we simulate dynamic tensile fracture and damage generation at the molecular level in -quartz, an abundant mineral in the Earth's continental crust, to quantify how rupture speed controls crack branching and damage production. Because this mineral requires a more detailed molecular potential than the Morse pair potential or the biharmonic potential used in previous studies (Zhou et al., 1996; Buehler and Gao, 2006), we use the Vashishta potential (Vashishta et al., 1990), which has been designed to reproduce the properties of crystalline quartz (Broughton et al., 1997). Our results quantify a mechanism of strain energy dissipation and damage production at the nanoscale throughout the tensile region of a fault zone during coseismic loading.

2 Methods

2.1 Simulation setup and procedure

The setup consists of a three-dimensional block of -quartz with a pre-cracked notch structure (Figure 1a). The block is cut along three crystallographic planes, and the orientation of the system (Figure 1b) is such that the xy plane (z-cut) corresponds to the (0 0 0 1) crystallographic plane, the yz plane (x-cut) is the ($\overline{2}$ 1 1 0) crystallographic plane and the xz plane (y-cut) is the (0 $\overline{1}$ 1 0) crystallographic plane. The system is periodic in the y-direction, while the boundaries at top, bottom and both ends in the x-direction are fixed in order to apply a specific stress state.

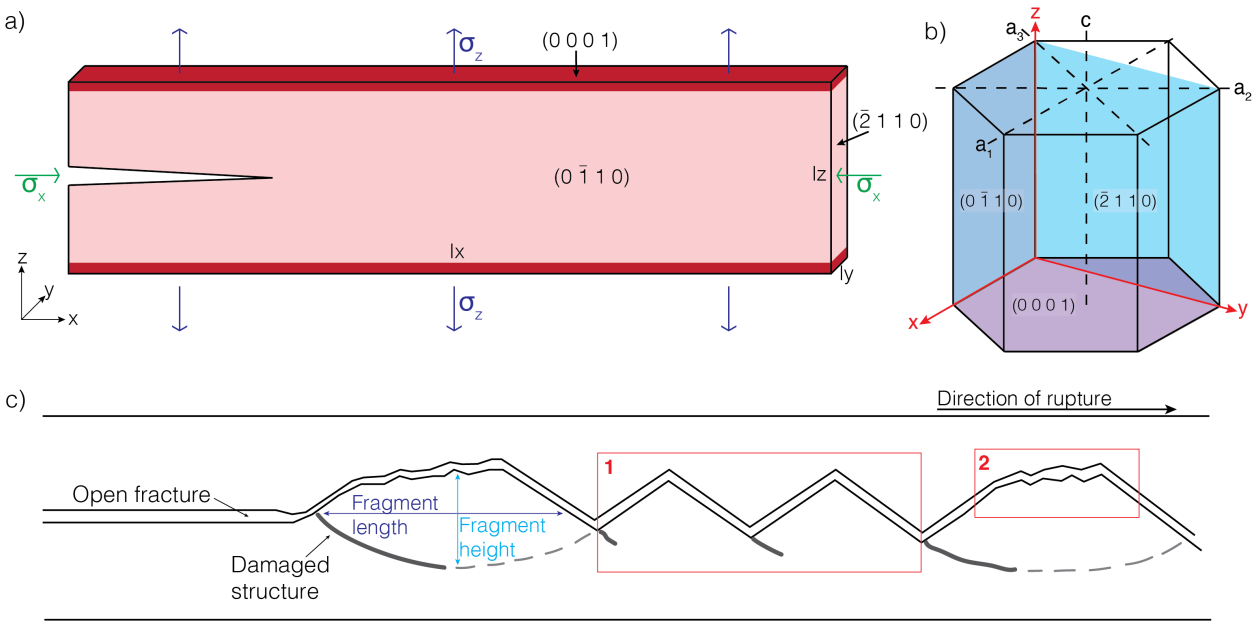

Figure 1. **a)** Sketch of the simulation setup. The slab is made of -quartz and contains a notch that guides tensile fracture propagation. The domain is a three-dimensional block dimensions l_x=300 nm, l_y=12 nm, and l_z=60 nm. The length of the initial notch is 60 nm, and the aperture is 16 Å on the left side. The upper and lower parts of the block (red areas) are fixed. The block is exposed to a compressive normal stress along the x-direction (σ_x), followed by a tensile strain along the z-direction (σ_z). **b)** Orientation of the block with a x-, y- and z-cut. Both the crystallographic axes (a_1, a_2, a_3 and c) and the coordinates axes (x, y, and z) used in our simulations are shown. **c)** A sketch of a fracture, drawn from a simulation snapshot. Solid lines represent observed damage while the dashed line represent potential damage at the atomic scale. Box 1 (red) illustrates a propagation path influenced by the crystallographic structure (see also Figure 2d), whereas box 2 (red) illustrates an area where the propagation path is less influenced by the crystallographic structure (see also Figure 2e).

First, a compressive normal stress is imposed along the x-direction using an isothermal-isobaric thermostat (NPT). Then, an extensional displacement controlled by the canonical ensemble (NVT) is imposed along the z-direction, perpendicularly to the notch. The imposed tensile strain leads to an initial tensile stress in the range 1000-2000 MPa, and the stress is measured just before the crack starts to propagate. These levels of tensile stress agrees with expectations for dynamic rupture propagation in the crust (e.g., Reches and Dewers, 2005). For most simulations, the -quartz block has dimensions 300x12x60 nm, the imposed compressive stress in the x-direction is 500 MPa, the extensional displacement along the z-axis is imposed over a period of 30 ps, and the temperature is set to 300 K.

The simulations are run for 500 ps with a time step of 1 fs, during which a tensile (mode I) dynamic crack propagates. During this time, depending on the initial tensile stress imposed on the system, one of three outcomes are observed: 1) the crack does not propagate from the initial notch; 2) the crack starts propagating and stops inside the simulation domain; or 3) the crack propagates throughout the simulation domain along the x-direction. If the crack does not propagate, the simulation is discarded because the loading was insufficient for dynamic crack propagation. If the crack propagates, but does not cross the whole domain, we increase the duration of the simulation such that the crack reaches the end of the simulation domain. Thus, we obtain a set of simulations where a crack has propagated throughout the entire system. We sample the position of the crack tip in the x-direction through time and calculate the average rupture speed. To assess the sensitivity of the rupture speed on the details of the simulation setup, we varied the loading plane, compressive stress, temperature, and loading rate. The effect of these variables on the rupture speed is described in the Supplementary Information, but overall the rupture speed is not particularly sensitive to these parameters and we observe the same qualitative behavior.

2.2 Interatomic interaction potential for -quartz

We perform the simulations using the molecular dynamics package LAMMPS (Plimpton, 1995). We model an -quartz with the interatomic potential initially defined by Vashishta et al. (1990) using the updated parametrization from Broughton et al. (1997). The 1997-version of the potential is modified from the Nakano et al. (1994) three-body potential, which was modified from the original version of the potential (Vashishta et al., 1990). The first versions of the potential were designed to reproduce the properties of molten, crystalline, and amorphous silica. Broughton et al. (1997) adjusted three parameters to optimize the material properties towards those of crystalline -quartz. Tables S1 and S2 display the parameters used in the simulations.

The 1997-version of the Vashishta potential reproduces the anisotropy of -quartz, including the elastic parameters and the compressibility of the lattice lengths. To ensure that the simulated material has properties similar to -quartz within the pressure and temperature range of our simulations, we have calculated the elastic parameters at T=1 K and P=0.1 MPa (Table S3), the density in a temperature range 1-520 K at 0.1 MPa and in a pressure range 0-10 GPa at 298 K, as well as the compressibility parameters of the lattice along different crystalline directions (a_1 and c) at 298 K in a pressure range 0-3 GPa (see Supplementary Information). Overall, when the applied pressure is below 3 GPa, the compressibility along the x- and z-axis, corresponding respectively to the crystallographic a_1-axis and c-axis, agrees with experimental studies (Jorgensen, 1978; d'Amour et al., 1979; Hazen et al., 1989; Glinnemann et al., 1992). The density of our simulated material is consistent with the density of -quartz in the temperature range 1-520 K. At 298 K, the density ( ) is slightly lower, but has a similar d /dP-slope in the range 0-3 GPa, which is within the range of our simulations, while it deviates at higher pressures (Figure S3). Based on

the elastic parameters (Table S3) and the density, the Rayleigh wave speed is 3048 m/s when applying an extensional displacement on the (0 0 0 1) plane and 3097 m/s when applying an extensional displacement on the (0 $\overline{1}$ 1 0) plane, using the procedure of Vinh and Ogden (2005). For comparison, Leong et al. (2018) measured the Rayleigh wave speed to be 3841 m/s when applying an extensional displacement on the (5 $\overline{10}$ 5 8) plane and 3694 m/s when applying an extensional displacement on the (1 $\overline{2}$ 1 3) plane. The difference between our measured speeds and the speeds reported by Leong et al. (2018), apart from different loading planes, is that the modelled material is slightly softer, as indicated by the elastic parameters (Table S3).

3 Results

For all the simulations, we describe the fracture surface roughness after the crack has propagated through the simulation domain by classifying the fracture geometry as straight cracks, oscillating cracks, and cracks exhibiting microbranching (Figure 2). When oscillations occur, we measure the amplitude of these oscillations (Figure 2f). For the straight cracks (Figure 2a), the propagation produces a combination of mirror and mist surface roughness. In some areas, the crack propagates along a single atomic plane, producing a mirror surface (Figure 2a, box 1). In other areas, the crack propagation creates a mist surface, by shifting between atomic layers (Figure 2a, box 2). Wherever the crack changes course or turns abruptly (Figure 2d), or where the crack branches (Figure 2e), damage is created in the surrounding quartz structure. The damage is characterized by a lower atomic density, and for a critical atomic distance of 1.9 Å, the coordination of silicon and oxygen atoms decreases from 4 and 2 in -quartz to 3 and 1 in damaged quartz.

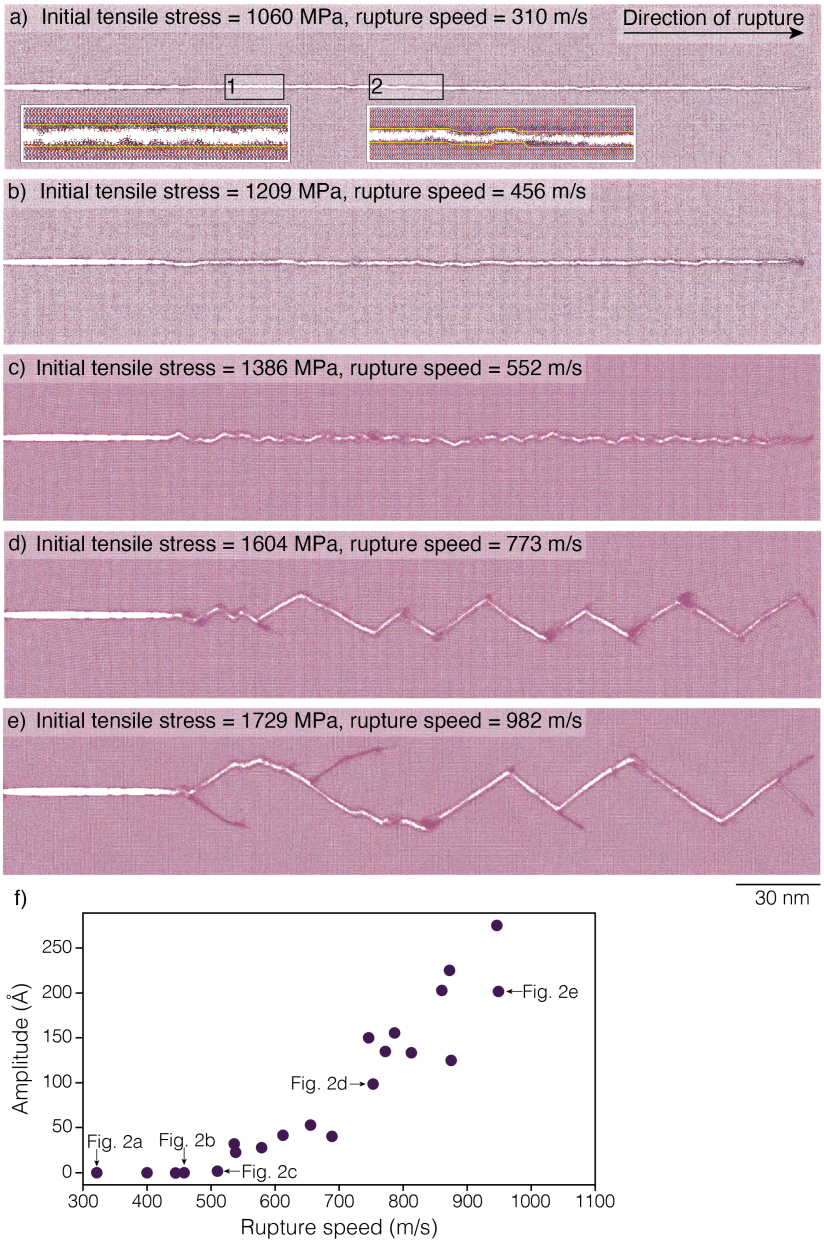

Figure 2. Snapshots of the atoms in the simulation system with a fracture (white) and damage (dark red) after the crack has propagated through -quartz. The darker red colored areas and areas with microbranching correspond to damage in the quartz structure by breakage of the atomic bonds. a) With an initial tensile stress of 1060 MPa, the crack propagates along an atomic plane. Area 1 shows a mirror surface, while area 2 shows mist. The yellow lines in the inset fig-

ures indicate the atomic layer along which the fracture propagates. b) With an initial tensile stress of 1209 MPa, the crack propagates mostly straight. c) With an initial tensile stress of 1386 MPa, the crack oscillates out-of-plane (hackle pattern). d) With an initial tensile stress of 1604 MPa, crack oscillations induce a more pronounced surface roughening. e) With an initial tensile stress of 1729 MPa, crack branching occurs. f) Amplitude of the oscillations as a function of rupture speed.

We measure the rupture speed in every simulation by sampling the position of the crack tip in the x-direction through time and identify the critical speed for crack oscillations and branching. Figure 3a shows how rupture speed and crack path vary with the initial tensile stress imposed on the system. Based on observations of features (Figure 2a-e), a qualitative difference is observed between Figure 2b and c. In Figure 2b, the crack propagates mostly straight but jump between layers, while in Figure 2c, it never propagates straight. This change in propagation behavior is observed when the initial tensile stress is around 1210 MPa and the rupture speed remains below 460 m/s, equivalent to $0.15C_{\mathrm{R}}$ (Figure 3a). When the initial tensile stress increases, the rupture speed increases as well, and the crack oscillates (Figure 2c-d). For initial tensile stresses larger than 1600 MPa, crack microbranching occurs, and the rupture speed exceeds 800 m/s, corresponding to $0.26C_{\mathrm{R}}$ (Figure 3a). During a branching event, two cracks propagate simultaneously until one of the cracks dominates, from which the dynamic rupture continues propagating (Figure 2e). In Figure 3a, we observe that slope of the rupture speed versus initial tensile stress is steepest before oscillations occur. However, when approaching an initial tensile stress where oscillations occur, the rupture speed stagnates before it continues to increase, indicating that there is an energy barrier to overcome before the crack starts to oscillate. Similarly, a stagnation of the cuve is observed around the threshold speed where microbranches start developing.

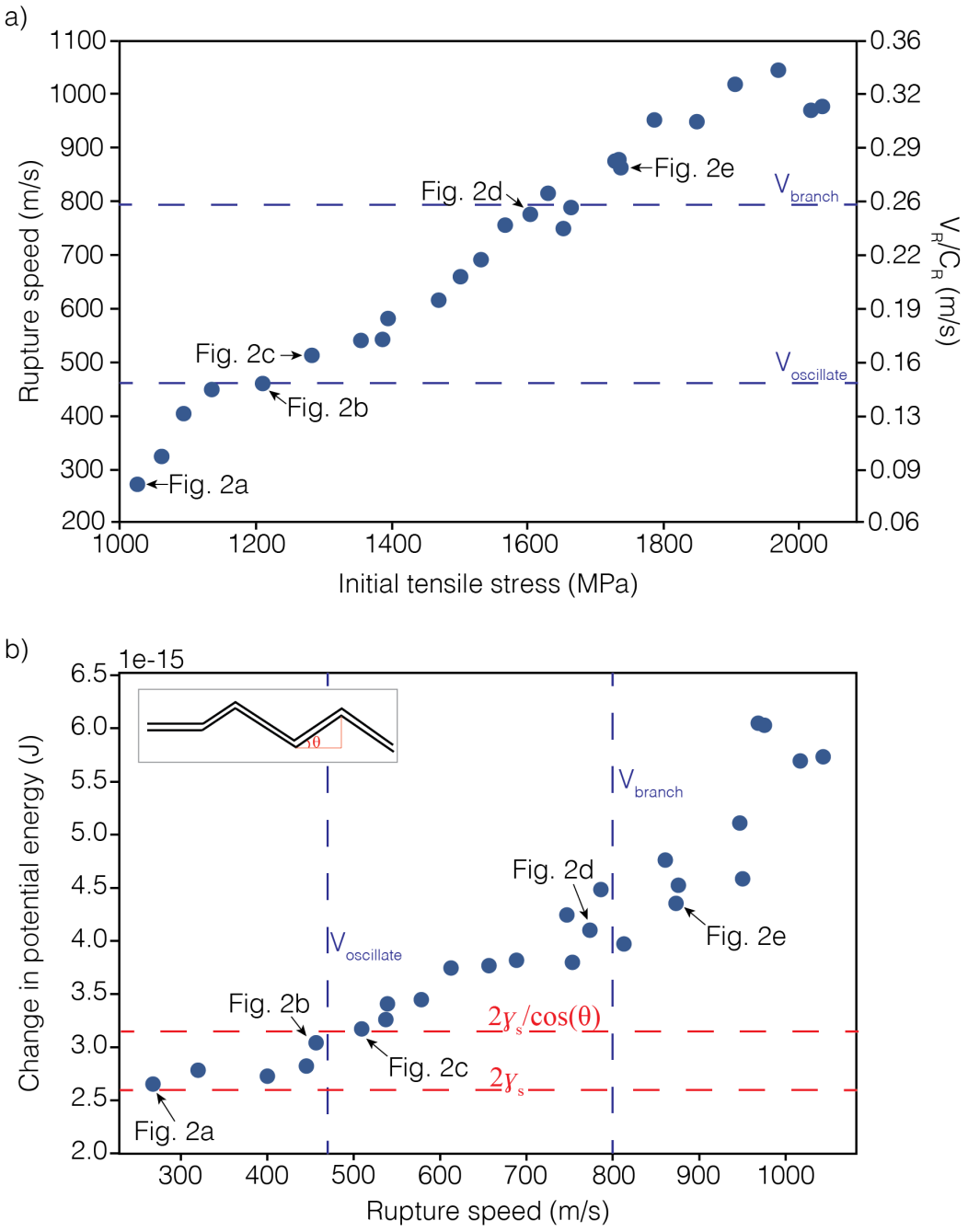

Figure 3. a) Rupture speed (V_{R}) of the crack tip as a function of initial tensile stress. Above a critical speed $V_{\mathrm{oscillate}} = 0.15\mathrm{C_R}$, where C_{R} is the Rayleigh wave speed, the crack tip oscillates. Above a critical speed $V_{\mathrm{branch}} = 0.26\mathrm{C_R}$, crack

branching occurs. b) Change in potential energy of the simulation domain from the relaxed initial system and the relaxed state after the crack has propagated through the domain, as a function of rupture speed. $_s$ is the surface energy.

The perfect quartz lattice is an energy minimum for our system. One way to characterize the damage caused by crack propagation is to compare the potential energy of the relaxed initial system with the potential energy of the relaxed state after the crack has propagated through the system. To obtain high crack speeds, the system has to be loaded substantially above the fracture toughness of the material, and this leads to thermal energy being released during crack propagation. This energy is absorbed by the thermostat during and after crack propagation and we make sure to measure the potential energy at the same temperature for the initial state and the cracked state. The potential energy is averaged over the last 50 ps of each simulation, and this averaging window starts at least 5 ps after the crack has reached the far end of the sample. For a perfectly straight crack, this energy difference should be equal to $2A\ _{s,}$ where $_s$ is the surface energy of a flat crack surface and A is the surface area of the new crack. In our simulations, the surface energy for straight cracks was measured by dividing the change in potential energy over the crack surface area, and found to be equal to 0.93 J/m^2. For comparison, the surface energy of the (0 0 0 1) plane of quartz in air has been measured experimentally to be 0.92 J/m^2 (Parks, 1984). Figure 3b shows how the dissipated energy varies with rupture speed. The results show that the energy dissipated in the system increases with increasing rupture speed due to fracture oscillation and microbranching that damages the material. The contribution of potential energy of new surfaces and damaged quartz structures varies for the oxygen and silicon atoms (Figures S10a and S11a). For the silicon atoms, the new surfaces provide a higher potential energy than the damaged structures. Conversely, for the oxygen atoms, the energy in the new surfaces is lower than in the damaged structure. This can be explained by the energy from the steric repulsion and the Coulomb interactions between oxygen pairs (see Supplementary Information).

4 Discussion

4.1 Morphology of the fracture surface

Fracture surfaces have been studied extensively in brittle materials, like polymethyl methacrylate (e.g., Fineberg et al., 1991; Sharon and Fineberg, 1996), Homalite (Ravi-Chandlar and Knauss, 1984), silica glass (Sharon and Fineberg, 1998) or neo-Hookean brittle gels (Livne et al., 2005). These studies showed that, above a threshold rupture speed, the crack surface changed from smooth to a jagged structure that undergoes instabilities characterized by either oscillations or microbranching. Our results show that the morphology of a crack surface in a model -quartz varies with rupture speed. At low speeds, the crack is propagating straight (Figure 2a). When the rupture speed increases, the crack undergoes path instabilities first by oscillations, where the amplitude of the oscillations increases as the crack speed increases (Figures 2c, d and f) and then, at higher rupture speeds by branching (Figure 2e).

Because polymethyl methacrylate is an amorphous material, Fineberg et al. (1991) and Sharon and Fineberg (1996) argued that the source of the observed oscillations in the experiments could not be linked to the material structure. Instead, the occurrence of the oscillations was attributed to a sudden increase in rupture speed. In contrast to an amorphous material, we observe that fracture propagation is controlled by the crystalline structure of -quartz to some degree. For example, the atom layers control the transition from mirror to mist surface as the crack jumps between different layers. At the onset of oscillations, the oscillations have a small amplitude and are irregular; they do not seem to follow the crystalline structure (e.g., Figure 2c). However, when the oscillations reach a more regular amplitude, they follow the crystalline structure of quartz (e.g., Figures 1c and 2d). During microbranching, certain areas with oscillations are controlled by the crystalline structure while, in other areas, zones of damage show a slightly rounded shape (Figure 1c), which cannot be directly linked to the crystalline structure of -quartz.

4.2 Rupture velocity and crack instabilities

The threshold speed above which path instabilities are observed has been measured in several materials and found to be in the range 0.3-0.74C_{R} (e.g., Zhou et al., 1996; Buehler and Gao, 2006; Bleyer and Molinari, 2017), and experiments on single-crystal quartz observed branching when the crack approached $0.45C_{\mathrm{R}}$ (Leong et al., 2018). In our simulations, we have identified two threshold speeds: $V_{\mathrm{oscillate}}$=$0.15C_{\mathrm{R}}$ is the speed of the first path instability that produces oscillations, and V_{branch}=$0.26C_{\mathrm{R}}$ is the speed at which the first microbranching is observed. These two speeds are slightly lower than experimental measurements performed in quartz on larger samples and significantly lower than the theoretical limit of C_{R}. In the next paragraph, we argue that this difference is controlled by the functional form of the cohesive force between silicon and oxygen atoms.

Buehler and Gao (2006) modeled an elastic 2D material and tuned the cohesive force between interacting atoms to study how this parameter controls rupture speed. The cohesive force is dependent on the breaking of atomic bonds, which occurs at a critical atom separation (r_{break}). This critical atom separation can be expressed as the ratio between the interatomic distance where the potential energy slope is steepest, and the minimum potential energy. It is one of the key parameters governing the crack instability speed. When r_{break}=1.135, a dynamic instability can occur for rupture velocities below $0.2C_{\mathrm{R}}$, while when r_{break} increases to 1.25, a dynamic instability occurs for rupture velocities above $0.73C_{\mathrm{R}}$. In the interatomic potential used in our simulations, r_{break} for the two-body interactions between silicon and oxygen atoms is equal to 1.144 (Figure S1). This value falls in the lower range of investigated r_{break} parameters (Buehler and Gao, 2006) and is consistent with the threshold speeds for crack propagation instabilities in the range 0.15-0.32C_{R} observed in our simulations. It is therefore likely that the shape of the two-body interaction between silicon and oxygen, and in particular the critical separation r_{break} governs the rupture speed. In future adjustments of the parameters of silica potentials, one should therefore

consider this quantity explicitly.

4.3 Production of damage during dynamic rupture

Damage zones in faults contain a high density of fractures at all scales, which may be created by several processes occurring during or after the fault formation, such as Andersonian fracturing, early fault tip migration, fault tip linkage (e.g., Johri et al., 2014; Mitchell and Faulkner, 2009), and dynamic ruptures (Rudnicki, 1980; Wilson et al., 2003; Paul et al., 2007). Models of dynamic rupture calculate the stress field around a fault tip during propagation, which allows quantifying the damage along the length of the rupture (e.g., Madariaga, 1976; Andrews, 1976). Our simulations indicate that a propagating tensile crack creates nanoscale damage. This damage is generated in the material surrounding the propagating crack and aborted branches, or in areas where oscillations shifts direction during propagation (e.g., Figure 2d).

Another type of damage produced by dynamic rupture is pulverized rocks, which have been shattered *in situ* without significant shear strain. These rocks consist of very fine grains (e.g., Dor et al., 2006). If our damaged crystal were exposed to further strain through shear deformation, this would lead to the formation of nanosized fragments (Figure 1c). In the simulations where rupture propagation produces microbranches, we have measured the height and length of nascent fragments. Independently of initial tensile stress, the height of the fragments would be around 20 nm, while their length would vary in the range 40-110 nm. For cracked grains in a gouge, the lower limit for fragment diameter is reported to be 30 nm; however, the fragments can also reach sizes up to 100 µm (Keulen et al., 2007). For grain sizes below 1.2 $\pm$ 0.3 µm, Keulen et al. (2007) proposed that these grains are produced by another mechanism than grinding. Sammis and Ben-Zion (2007) explored mechanisms that might produce fragment below the grinding limit. These authors showed that nanometer-sized fragments rarely form by grain crushing in simple shear under compressive loading, but could be produced during tensile loading at high strain rates. An estimate of the smallest fragment produced by tensile stress can be found by $\mathbf{K}_{\mathrm{IC}} = \sqrt{\mathrm{a}}$, where K_{IC} is the fracture toughness and 1 MPa $\mathrm{m}^{1/2}$ for quartz (e.g., Iwasaki and Torikai, 1993), is the tensile stress and a is the radius of the flaw. In our simulation, the tensile stress is in the range 1-2 GPa, which will give a=80-320 nm. If the flaws are almost equal in size and distributed uniformly in the rock, a will indicate the dimensions of the fragments, otherwise even smaller fragments could be formed (Sammis and Ben-Zion, 2007). From our simulations, even the longest fragments (110 nm) are much smaller than the grinding limit for quartz and in the lower range of estimated fragment sizes due to tensile loading condition. Therefore, dynamic rupture at molecular scale could provide an explanation for the formation of rock fragments with dimensions smaller than the grinding limit. This is supported by Wilson et al. (2005) who argued that the smallest fragments in gouges might be explained by damage from a crack tip during dynamic rupture.

5 Conclusion

We perform molecular scale simulations of dynamic rupture propagation in -quartz loaded under tensile stress. We identify critical rupture speeds for crack oscillations and crack branching consistent with results from Gao and Buehler (2006). When the rupture speed is below 460 m/s, the crack propagates straight, while at speeds above 460 m/s, it starts oscillating. This rupture speed corresponds to $0.15C_{\mathrm{R}}$. For microbranching to occur, the rupture speed must exceed 800 m/s, which corresponds to $0.26C_{\mathrm{R}}$. During a crack branching event, two branches propagate simultaneously until one branch dominates. These two branches may provide an initial structure that could lead to quartz nanosized fragments with dimensions below the grinding limit. These fragments in fault damage zones have a high surface area and thus may react relatively fast in the presence of aqueous fluids, leading to fast fault healing and strength recovery.

Acknowledgments

We thank Fabian Barras and Jessica McBeck for useful and constructive suggestions on an early version of the manuscript. The Research Council of Norway funded this study (project History Dependent Friction 287084).

Data Availability Statement

All research data and numerical codes necessary to reproduce the results of the study are available from Zenodo at https://doi.org/ 10.5281/zenodo.5873712.

References

Abraham, F. F., Brodbeck, D., Rudge, W. E., & Xu, X. (1997). A molecular dynamics investigation of rapid fracture mechanics. *Journal of the Mechanics and Physics of Solids*, *45*(9), 1595–1619.

Andrews, D. J. (1976). Rupture Propagation With Finite Stress in Antiplane Strain. *Journal of Geophysical Research*, *81*(20), 3575–3582.

Andrews, D. J. (2005). Rupture dynamics with energy loss outside the slip zone. *Journal of Geophysical Research: Solid Earth*, *110*(1), 1–14.

Ben-Zion, Y., & Shi, Z. (2005). Dynamic rupture on a material interface with spontaneous generation of plastic strain in the bulk. *Earth and Planetary Science Letters*, *236*(1–2), 486–496.

Bleyer, J., & Molinari, J. F. (2017). Microbranching instability in phase-field modelling of dynamic brittle fracture. *Applied Physics Letters*, *110*(15), 151903.

Bouchbinder, E., Goldman, T., & Fineberg, J. (2014). The dynamics of rapid fracture: Instabilities, nonlinearities and length scales. *Reports on Progress in Physics*, *77*(4), 046501.

Broughton, J. Q., Meli, C. A., Vashishta, P., & Kalia, R. K. (1997). Direct atomistic simulation of quartz crystal oscillators: Bulk properties and nanoscale devices. *Physical Review B - Condensed Matter and Materials Physics*, *56*(2), 611–618.

Buehler, M. J., & Gao, H. (2006). Dynamical fracture instabilities due to local hyperelasticity at crack tips. *Nature*, *439*(7074), 307–310.

Buehler, M. J. (2008). *Atomistic modeling of materials failure*. Springer Science & Business Media.

d'Amour, H., Denner, W., & Schulz, H. (1979). Structure determination of -quartz up to 68 x 108 Pa. *Acta Crystallographica Section B: Structural Crystallography and Crystal Chemistry*, *35*(3), 550–555.

Di Toro, G., & Pennacchioni, G. (2005). Fault plane processes and mesoscopic structure of a strong-type seismogenic fault in tonalites (Adamello batholith, Southern Alps). *Tectonophysics*, *402*(1-4 SPEC. ISS), 55–80.

Doan, M. L., & Gary, G. (2009). Rock pulverization at high strain rate near the SanAndreas fault. *Nature Geoscience*, *2*(10), 709–712.

Dor, O., Ben-Zion, Y., Rockwell, T. K., & Brune, J. (2006). Pulverized rocks in the Mojave section of the San Andreas Fault Zone. *Earth and Planetary Science Letters*, *245*(3–4), 642–654.

Fineberg, J., Gross, S. P., Marder, M., & Swinney, H. L. (1991). Instability in dynamic fracture. *Physical Review Letters*, *67*(4), 457–460.

Glinnemann, J., King Jr, H. E., Schulz, H., Hahn, T., La Placa, S. J., & Dacol, F. (1992). Crystal structures of the low-temperature quartz-type phases of SiO2 and GeO2 at elevated pressure. *Zeitschrift Für Kristallographie-Crystalline Materials*, *198*(1–4), 177–212.

Guren, M.G. (2022). Supplementary data for "Nanoscale modelling of dynamic rupture and damage generation in alpha-quartz" [Data set]. Zenodo. https://doi.org/10.5281/zenodo.5873712

Hazen, R. M., Finger, L. W., Hemley, R. J., & Mao, H. K. (1989). High-pressure crystal chemistry and amorphization of -quartz. *Solid State Communications*, *72*(5), 507–511.

Iwasaki, H., & Torikai, D. (1993). Thermal shock of quartz lascas. *Journal of Materials Science*, *28*(19), 5223–5228.

Johri, M., Dunham, E. M., Zoback, M. D., & Fang, Z. (2014). Predicting fault damage zones by modeling dynamic rupture propagation and comparison with field observations. *Journal of Geophysical Research: Solid Earth*, *119*, 1251–1272.

Jorgensen, J. D. (1978). Compression mechanisms in -quartz structures—SiO2 and GeO2. *Journal of Applied Physics*, *49*(11), 5473–5478.

Kendall, K. (1978). The impossibility of comminuting small particles by compression. *Nature*, *272*(5655), 710–711.

Keulen, N., Heilbronner, R., Stünitz, H., Boullier, A. M., & Ito, H. (2007). Grain size distributions of fault rocks: A comparison between experimentally

and naturally deformed granitoids. *Journal of Structural Geology*, *29*(8), 1282–1300.

Leong, A. F. T., Robinson, A. K., Fezzaa, K., Sun, T., Sinclair, N., Casem, D. T., Lambert, P. K., Hustedt, C. J., Daphalapurkar, N. P., & Ramesh, K. T. (2018). Quantitative in situ studies of dynamic fracture in brittle solids using dynamic X-ray phase contrast imaging. *Experimental Mechanics*, *58*(9), 1423–1437.

Livne, A., Cohen, G., & Fineberg, J. (2005). Universality and hysteretic dynamics in rapid fracture. *Physical Review Letters*, *94*(22), 224301.

Madariaga, B. Y. R. (1976). Dynamics of an expanding circular fault. *Bulletin of the Sesimological Society of America*, *66*(3), 639–666.

Mitchell, T. M., & Faulkner, D. R. (2009). The nature and origin of off-fault damage surrounding strike-slip fault zones with a wide range of displacements: A field study from the Atacama fault system, northern Chile. *Journal of Structural Geology*, *31*(8), 802–816.

Muto, J., Nakatani, T., Nishikawa, O., & Nagahama, H. (2015). Fractal particle size distribution of pulverized fault rocks as a function of distance from the fault core. *Geophysical Research Letters*, *42*(10), 3811–3819.

Nakano, A., Kalia, R. K., & Vashishta, P. (1994). First sharp diffraction peak and intermediate-range order in amorphous silica: finite-size effects in molecular dynamics simulations. *Journal of Non-Crystalline Solids*, *171*(2), 157–163.

Parks, G. A. (1984). Surface and interfacial free energies of quartz. *Journal of Geophysical Research: Solid Earth*, *89*(B6), 3997–4008.

Paul, P. K., Zoback, M. D., & Hennings, P. H. (2007). Fluid Flow in a Fractured Reservoir Using a Geomechanically-Constrained Fault Zone Damage Model for Reservoir Simulation. In *SPE Annual Technical Conference and Exhibition* (p. SPE-110542-MS).

Petley-Ragan, A., Ben-Zion, Y., Austrheim, H., Ildefonse, B., Renard, F., & Jamtveit, B. (2019). Dynamic earthquake rupture in the lower crust. *Science Advances*, *5*(7), 1–8.

Plimpton, S. (1995). Fast Parallel Algorithms for Short – Range Molecular Dynamics. *Journal of Computational Physics*, *117*(1), 1–19.

Prasher, C. L. (1987). *Crushing and grinding process handbook*. Wiley, New York.

Ravi-Chandar, K., & Knauss, W. G. (1984). An experimental investigation into dynamic fracture: II. Microstructural aspects. *International Journal of Fracture*, *26*(1), 65–80.

Reches, Z., & Dewers, T. A. (2005). Gouge formation by dynamic pulverization during earthquake rupture. *Earth and Planetary Science Letters*, *235*(1–2),

361–374.

Rempe, M., Mitchell, T., Renner, J., Nippress, S., Ben-Zion, Y., & Rockwell, T. (2013). Damage and seismic velocity structure of pulverized rocks near the San Andreas Fault. *Journal of Geophysical Research: Solid Earth*, *118*(6), 2813–2831.

Rudnicki, J. W. (1980). Fracture mechanics applied to the Earth's crust. *Annual Review of Earth and Planetary Sciences*, *8*, 489–525.

Sammis, C., King, G., & Biegel, R. (1987). The kinematics of gouge deformation. *Pure and Applied Geophysics*, *125*(5), 777–812.

Sammis, C. G., & Ben-Zion, Y. (2008). Mechanics of grain-size reduction in fault zones. *Journal of Geophysical Research: Solid Earth*, *113*(2), 1–12.

Sharon, E., & Fineberg, J. (1996). Microbranching instability and the dynamic fracture of brittle materials. *Physical Review B - Condensed Matter and Materials Physics*, *54*(10), 7128–7139.

Sharon, E., & Fineberg, J. (1998). Universal features of the microbranching instability in dynamic fracture. *Philosophical Magazine B*, *78*(2), 243–251.

Vashishta, P., Kalia, R. K., Rino, J. P., & Ebbsjö, I. (1990). Interaction potential for SiO 2: A molecular-dynamics study of structural correlations. *Physical Review B*, *41*(17), 12197.

Vinh, P. C., & Ogden, R. W. (2005). On the Rayleigh wave speed in orthotropic elastic solids. *Meccanica*, *40*(2), 147–161.

Wilson, J. E., Chester, J. S., & Chester, F. M. (2003). Microfracture analysis of fault growth and wear processes, Punchbowl Fault, San Andreas system, California. *Journal of Structural Geology*, *25*(11), 1855–1873.

Wilson, B., Dewers, T., Reches, Z., & Brune, J. (2005). Particle size and energetics of gouge from earthquake rupture zones. *Nature*, *434*(7034), 749–752.

Zhou, S. J., Lomdahl, P. S., Thomson, R., & Holian, B. L. (1996). Dynamic crack processes via molecular dynamics. *Physical Review Letters*, *76*(13), 2318–2321.